Model Predictive Control of Time-Varying Aberrations for Sensorless Adaptive Optics

Jinsung Kim, Kye-Sung Lee, Sang-Chul Lee, Ji Yong Bae, Dong Uk Kim, I. Jong Kim, Ki Soo Chang, and Hwan Hur

Abstract— We propose a model predictive control (MPC) method to compensate for the time-varying phase aberrations in a sensorless adaptive optics (AO) system. The approximate model for the point spread function (PSF) of the imaging system with phase diversity is mathematically derived, and its validity is verified. The proposed MPC, which considers the operating limits of the deformable mirror (DM), computes the optimal applied voltage of each actuator over a prediction horizon, and the receding horizon scheme is applied as feedback control. Numerical case studies with the time-varying phase aberrations generated by an atmospheric turbulence simulator are presented to demonstrate the correction performance of the MPC strategy. The proposed method caused a 50% improvement in the reduction in residual aberration, making it competitive with a saturation linear quadratic regulator (LQR). The computational feasibility of the proposed method is validated using fast MPC, which approximates the primal barrier method.

Index Terms— Model identification, model predictive control (MPC), phase diversity, phase retrieval method, point spread function (PSF), sensorless adaptive optics (AO).

I. INTRODUCTION

ATMOSPHERIC turbulence or nonuniform refractive index distribution of a specimen can cause optical aberrations, which degrade the axial resolution and contrast of the image and limit the depth of focus. To eliminate these aberrations, adaptive optics (AO) has been introduced to generate a conjugated wavefront corresponding to the opposite component of the distorted wavefront. The AO system uses an adaptive element, such as a deformable mirror (DM) or spatial light modulator to correct aberrations and a control system that generates a signal to drive the adaptive element.

Based on an aberration measurement method, AO can be classified into direct wavefront measurement or indirect aberration optimization [1]. The direct method uses a Shack–Hartmann wavefront sensor to measure the spatial derivative of the wavefront. These sensors require a point-like

source of light and have disadvantages such as weak retroreflection and limited focal length [2]. To overcome these problems, sensorless AO based on the optimization algorithm measures aberrations using a sequence of images. The optimization algorithms can be divided into model-free and model-based algorithms. The former uses the blind optimization search algorithms such as stochastic parallel gradient descent [3], [4], genetic algorithms [5], and hill-climbing [6], [7]. It is challenging to implement the AO system in real-time since these blind methods require numerous measurements and iterations [8]. The model-based method, which uses physical modeling of the image quality metric, requires only $n + 1$ photodetector measurements to correct n aberration modes and has a faster convergence speed than the model-free method. Booth modeled the point source of the aberration using predetermined bias functions such as Zernike or Lukosz–Zernike polynomials according to the magnitude of aberrations [2], [9]. Meanwhile, a general model-based approach [10] is insensitive to a set of orthogonal modes selected as a bias function due to the approximately linear relationship between the second moment of the wavefront gradients and the masked detector signal. However, these model-based approaches are not suitable for the time-varying aberrations because they assume that aberrations are invariant while taking measurements.

To correct the time-varying phase aberration, we use a phase diversity technique with a known diversity function that retrieves the phase information of the wavefront using in-focus and out-of-focus images [11], [12], [13]. The main idea of the phase diversity method is to estimate the aberration from an approximate point spread function (PSF) model under the assumption that the magnitude of wavefront aberration is less than 0.5 rad rms [14], [15]. Many efforts have been undertaken to develop the phase diversity methods for wavefront correction. In [16], an iterative linear phase diversity method based on the first-order Taylor expansion of the PSF was proposed. A fast wavefront correction approach based on a linear phase diversity technique, applicable even for a highly strong atmospheric turbulence situation, was represented by [17] and [18]. However, these iterative linear phase diversity methods have been applied only for static aberrations as the aberrations should not change during the iterative correction process. In addition, it is necessary to assume that the frame rate of the imaging camera is sufficiently high and that the DM can fully compensate for the estimated residual
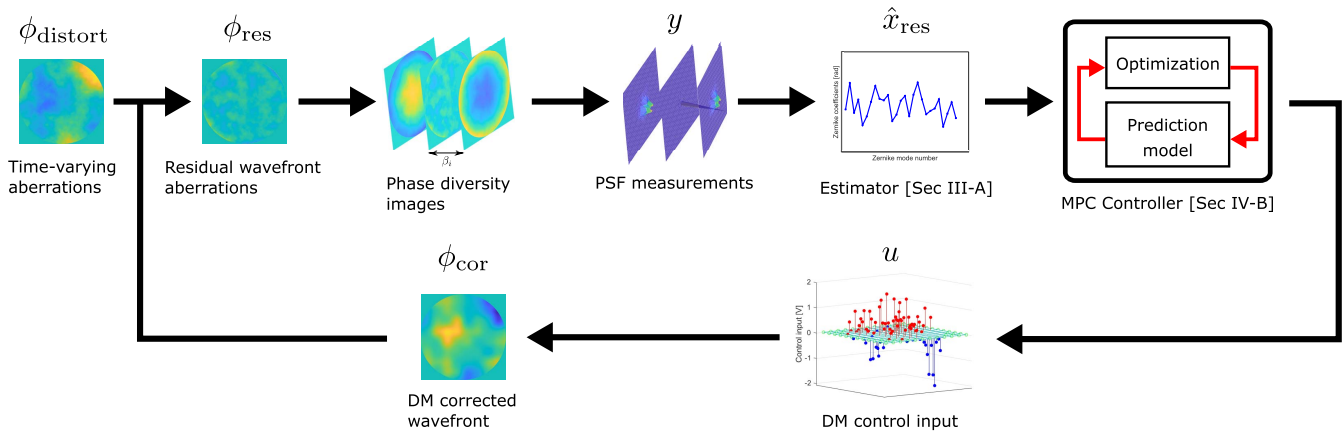
Fig. 1.   Flowchart illustrating the compensation of the time-varying aberrations for sensorless AO.

aberration. For the time-varying aberrations, many researchers have developed the temporal dynamics of aberrations and presented solutions based on various numerical approaches. Doelman *et al.* [19] presented a convex heuristic approach for blind system identification and estimated both phase aberration and temporal dynamics directly from the PSF assuming small-phase aberration. Marinica *et al.* [20] presented a method for estimating aberrations using an extended Kalman filter and correcting it with a linear quadratic regulator (LQR) based on an approximate model using the Kolmogorov turbulence spectrum. However, the control input determined using this method does not consider the stroke limitations of the DM.

The AO system control problem can be formulated as a finite-horizon constrained optimal control problem (OCP). The model predictive control (MPC) strategy solves this problem by approximating it over a prediction horizon [21], [22], [23], [24]. MPC is based on the receding horizon control (RHC) scheme and model-based batch predictions of the behaviors of controlled dynamic systems. A remarkable advantage of MPC is to achieve the stable operation of DM because input constraints can be implemented. In addition, a specific structure tailored to quadratic cost and linear dynamics can be applied using numerous open-source toolboxes, such as CVX and qpOASES. In [25], an MPC approach was used to compensate for aberrations while considering the physical constraints of the adaptive elements. However, the simulations were only implemented for exciting the AO system with sinusoids, and not the aberrations generated by atmospheric turbulence. Moreover, the computational burden of large-scale systems was not considered. Konnik and De Doná [26] used hot start and bound constraints in an active set quadratic programming (QP) algorithm to ensure the computational feasibility of constrained RHC for the AO control problem. However, a simple DM model was used, assuming weak coupling between actuators.

To overcome the limitations of the existing methods, we present an MPC method for sensorless AO. The proposed method satisfies the operating limits for all the actuators of the DM, and the receding horizon scheme is applied as a feedback control. The dynamic model of the time-varying aberrations is formulated as an autoregressive (AR) model based on a

time-series method. The proposed method is not limited to sensorless AO but can be scaled to optical systems using wavefront sensors. In addition, it is applicable to any type of dynamic aberration caused by the refractive index structure of the specimen or blood flow. To make it computationally feasible, autonomous coded or programmed algorithms and fast MPC [27], which approximates the primal barrier method, were used. A flowchart of the overall simulation for compensating the time-varying aberrations is illustrated in Fig. 1. For each time step, the time-varying phase aberration is combined with the wavefront corrected by the DM in the previous time step. The reflected beam with residual aberration is incident on a scientific camera to capture three phase diversity images, which can be simultaneously or sequentially captured, depending on the optical setup [28], [29]. Different PSFs are measured from three phase diversity images, and the Zernike coefficient for the residual wavefront aberrations is estimated using the least-squares method based on a first-order approximate model. The controller determines the optimal values of the DM actuator commands, and the DM is shaped to cancel out the majority of the distortion introduced in the next time step.

The remainder of this article is organized as follows: Section II describes the modeling of the AO system and time-varying aberrations. Moreover, the constrained OCP to compensate for aberrations is formulated. In Section III, a method for estimating the residual wavefront based on the PSF approximation model is presented. Section IV presents model identification based on the time-series method and the solution to the constrained OCP using MPC. In Section V, we illustrate the effectiveness of the proposed computational methods using a numerical case study with the time-varying phase aberrations. Finally, Section VI concludes the article with a perspective on future work.

II. MODELING OF THE OPTICAL SYSTEM

A schematic of the sensorless AO system is shown in Fig. 2. The incoming light with the time-varying phase aberration ϕ_{distort} caused by atmospheric turbulence is directed to the DM with a corrected wavefront ϕ_{cor}. The reflected beam with residual wavefront aberration $\phi_{\text{res}} = \phi_{\text{distort}} + \phi_{\text{cor}}$ is
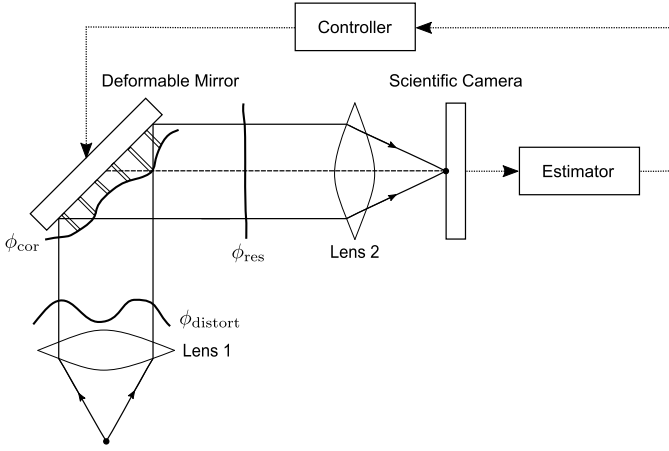
Fig. 2.   Schematic of sensorless AO setup.

Fig. 3. $4f$ optical system with phase diversity.

entered onto a scientific camera, such as a charge-coupled device (CCD) or complementary metal oxide semiconductor (CMOS), to measure the PSF. The estimator determines the Zernike coefficient constituting ϕ_{res} without using a wavefront sensor, based on the approximate model. The controller computes the voltage applied to each actuator of the DM to correct the aberration of the newly incoming light.

This section describes the modeling of the optical system components illustrated in Fig. 2 and the formation of a constrained OCP to correct the wavefront aberration.

A. Overview of AO System

The phase aberration of an input wavefront can be expressed as a series of n Zernike polynomials orthogonal to each other

$$\phi(\chi) = \sum_{r=1}^{n} \alpha_r Z_r(\chi) = \mathcal{Z}\alpha$$

where $\mathcal{Z} = [Z_1(\chi), \ldots, Z_n(\chi)] \in \mathbb{R}^{p^2 \times n}$ is a matrix that includes the n Zernike polynomials within a unit circle evaluated in the normalized pupil coordinates χ. p^2 is the total number of pixels, and $\alpha = [\alpha_1, \ldots, \alpha_n] \in \mathbb{R}^n$ are the Zernike coefficients. The order of the Zernike polynomial follows the America/American National Standards Institute (OSA/ANSI) standards [30]. Therefore, the phase retrieval problem can be solved by determining the Zernike coefficient corresponding to the phase aberration.

The phase diversity method uses modulated point-source images to recover the phase information of the distorted wavefront. The $4f$ optical system with phase diversity β_i is shown in Fig. 3. The black- and red-dashed lines indicate the focal plane and defocused plane, respectively. Defocus is commonly used as a diversity function because it has no angular dependence on the pupil coordinates and is straightforward to implement in an optical setup [31]. The phase aberration with defocus having a magnitude of β_i is represented by

$$\phi_i(\chi) = \sum_{r=1}^{n} \alpha_r Z_r(\chi) + \beta_i Z_5(\chi) = \mathcal{Z}\alpha + \beta_i Z_5(\chi).$$

The PSF $y(\zeta; \alpha, \beta_i)$ corresponding to the ith phase diversity is represented as the intensity of the Fourier transform of the
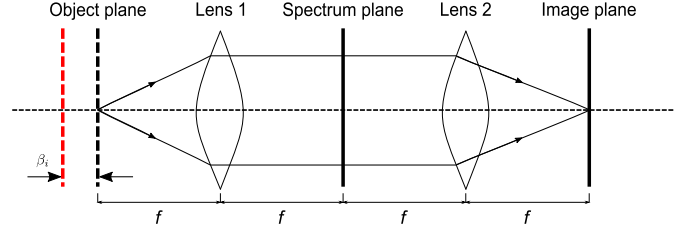
generalized pupil function (GPF) as follows:

$$y(\zeta; \alpha, \beta_i) = |\mathcal{F}(g(\chi; \alpha, \beta_i))|^2 + n_i \tag{1}$$

where ζ represents the image plane coordinates, and $\mathcal{F}(\cdot)$ is the 2-D Fourier transform. The GPF $g(\chi; \alpha, \beta_i) = \mathcal{A}(\chi)\exp(i\phi_i(\chi))$ is a complex-valued function, where $\mathcal{A}(\cdot)$ represents the amplitude apodization function, which is 1 inside the pupil and 0 outside the pupil. The measurement noise of the scientific camera $n_i \sim \mathcal{N}(0, \sigma_i)$ is the white Gaussian noise with standard deviation σ_i. For shorthand notation, we denote the PSF of the j-th pixel as $y_{i,j} := y_j(\zeta; \alpha, \beta_i) \; \forall j = 1, \ldots, p^2$. To estimate the Zernike coefficient for unknown aberration without using a wavefront sensor, various PSF approximation models have been proposed [32], [33]. Here, we define one based on the Taylor series expansion around zero aberration [16], [20], [34]

$$y_{i,j} = D_{0,j}(\beta_i) + D_{1,j}(\beta_i)\alpha + \frac{1}{2}\alpha^\top D_{2,j}(\beta_i)\alpha + \mathcal{O}(\|\alpha\|^3) \tag{2}$$

where

$$D_{0,j}(\beta_i) = y_j(\zeta; \alpha, \beta_i)\big|_{\alpha=0} \in \mathbb{R}$$
$$D_{1,j}(\beta_i) = \frac{\partial y_j(\zeta; \alpha, \beta_i)}{\partial \alpha}\bigg|_{\alpha=0} \in \mathbb{R}^n$$
$$D_{2,j}(\beta_i) = \frac{\partial^2 y_j(\zeta; \alpha, \beta_i)}{\partial \alpha \partial \alpha^\top}\bigg|_{\alpha=0} \in \mathbb{R}^{n \times n}$$

and $\mathcal{O}(\|\alpha\|^3)$ denotes terms of higher order than third degree. The Euclidean norm of a vector α is expressed as $\|\alpha\| = (\alpha_1^2 + \cdots + \alpha_n^2)^{1/2}$. Fig. 4 represents the root-mean-square error (RMSE) for the approximate model according to the magnitude of aberration. As the magnitude of aberration increases, the accuracy of the first-order approximation model decreases compared with that of the second-order model. The details of all the parameters constituting the approximate model are presented in Appendix A. Based on the first derivative $D_{1,j}(\beta_i)$ represented in [35], we mathematically derive the second derivative of the approximate model. Moreover, the computational burden was reduced by calculating the Jacobian and Hessian offline. The estimation method based on the first- and second-order approximation models is described in Section III.

B. Time-Varying Aberration Model

The temporal dynamics of the Zernike coefficient x_t constituting the time-varying phase aberration ϕ_{distort} can be
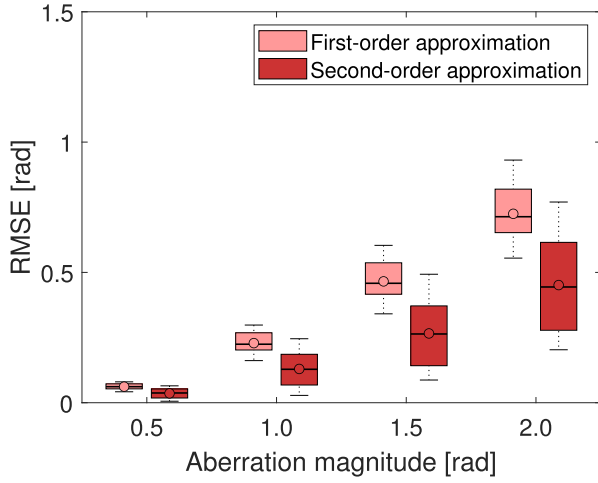
Fig. 4. Comparison of the RMSE for the approximate model according to the magnitude of aberration. The colored boxes indicate the 25th and 75th percentiles of the results in a Monte Carlo simulation.

represented by a vector-valued AR (VAR) model of order N_v as follows [19], [36]:

$$x_t[k] = f(x_t[k-1], \ldots, x_t[k-N_v], w[k])$$
$$= A_1 x_t[k-1] + \cdots + A_{N_v} x_t[k-N_v] + w[k] \quad (3)$$

where k represents the time index, $A_i \in \mathbb{R}^{n \times n} \; \forall i = 1, \ldots, N_v$ are the coefficient matrices, and $w[k] \sim \mathcal{N}(0, Q_w)$ is the white Gaussian noise. A detailed description of the method for obtaining the coefficient matrices is provided in Section IV-A.

C. DM Model

The wavefront corrected by the DM is represented by influence functions to each actuator as

$$\phi_{\text{cor}} = \sum_{j=1}^{m} I_j(\chi) u_j = \mathcal{I} u$$

where m is the number of actuators, $u = [u_1, \ldots, u_m]^\top \in \mathbb{R}^m$ are the applied voltage to each actuator, and $\mathcal{I} = \begin{bmatrix} I_1(\chi) & I_2(\chi) & \cdots & I_m(\chi) \end{bmatrix} \in \mathbb{R}^{p^2 \times m}$ are the DM influence matrix. In this study, $I_j(\chi)$ was designed as a Gaussian influence function [37], [38]

$$I_j(\chi) = \exp\left(\ln(c) \frac{(\chi - \chi_{0,j})^2}{d^2} \right)$$

where c is the coupling coefficient representing the influence of neighboring actuators, d is the distance between the actuators, and $\chi_{0,j}$ is the center coordinate of the jth actuator. If the DM is operated as a modal method, the corrected wavefront and influence functions are decomposed into a set of Zernike polynomials as follows [39]:

$$I_j(\chi) = \sum_{r=1}^{n} b_{r,j} Z_r(\chi).$$

In matrix representation, $\mathcal{I} = \mathcal{Z}B$, where the coefficient matrix $B \in \mathbb{R}^{n \times m}$, whose element is $b_{r,j}$, can be obtained using the least-squares method as $B = \mathcal{Z}^\dagger \mathcal{I}$. The notation $\dagger$ forms a

Moore–Penrose pseudoinverse of a matrix $\mathcal{Z}^\dagger = (\mathcal{Z}^\top \mathcal{Z})^{-1} \mathcal{Z}^\top$. Consequently, the Zernike coefficient constituting the corrected wavefront can be described by

$$x_{\text{cor}} = Bu. \quad (4)$$

The wavefront correction by the DM is denoted as $\phi_{\text{cor}} = \mathcal{Z} x_{\text{cor}}$. Therefore, the Zernike coefficient constituting the residual aberration is expressed as

$$x_{\text{res}} = x_t + x_{\text{cor}}. \quad (5)$$

D. Operating Constraints

In this study, we used an MEMS-based DM (Boston Micromachines Inc.) with 144 actuators in a 12×12 grid. The voltage applied to each actuator should be limited by the stroke limitations of the DM

$$u[k] \in [u_{\min}, u_{\max}].$$

If the time to attain the DM steady state is shorter than the sampling time of the control system, the settling time to reach the required large stroke may be delayed [40]. Therefore, we consider a ramp rate constraint to reduce the stress applied to each actuator of the DM as

$$u[k] - u[k-1] \in [\Delta u_{\min}, \Delta u_{\max}].$$

E. OCP Formulation

In this section, we propose a constrained OCP that determines the sequence of the optimal applied voltage $u^*[\cdot] := (u^*[0], \ldots, u^*[t_f - 1])$ to correct the time-varying phase aberrations. The objective function is defined in the quadratic form of residual aberration and control input as follows:

$$\min_{\{u[\cdot]\}} \sum_{k=1}^{t_f} \|x_{\text{res}}[k]\|^2 + \|u[k-1]\|^2$$
$$\text{s.t. } x_{\text{res}}[k] = x_t[k] + x_{\text{cor}}[k-1]$$
$$x_t[k] = f(x_t[k-1], \ldots, x_t[k-N_v], w[k])$$
$$u[k-1] \in [u_{\min}, u_{\max}]$$
$$u[k] - u[k-1] \in [\Delta u_{\min}, \Delta u_{\max}]$$
$$x_{\text{res}}[0] = \hat{x}_{\text{res}} \quad (6)$$

where t_f is the terminal time, and all the constraints must be satisfied for all the time indices $k = 1, \ldots, t_f$. The temporal dynamics of x_t and the relationship between x_{cor} and the control input are defined by (3) and (4), respectively. It is assumed that the equality constraint $x_{\text{res}}[0] = \hat{x}_{\text{res}}$ is obtained from the estimator because the initial state of the system cannot be directly measured in sensorless AO.

III. ABERRATION ESTIMATION

Because the sensorless AO does not use a wavefront sensor, the Zernike coefficient for the residual wavefront is estimated based on the PSF measured using the scientific camera. In this section, we describe a method for estimating the Zernike coefficients based on the PSF approximation model (2).

A. Least-Squares Method Based on the First-Order Approximate Model

The first-order Taylor series approximation of the PSF is the same as that of $D_{2,j}(\beta_i) = \mathbf{0}_n$ in (2), where the null matrix and identity matrix are denoted by $\mathbf{0}_n \in \mathbb{R}^{n \times n}$ and $\mathbf{I}_n \in \mathbb{R}^{n \times n}$, respectively. A vector representation of each pixel j for all the phase diversities $i = 1, \ldots, n_p$ is expressed as

$$y = b_s + A_s \alpha$$

where

$$y = \begin{bmatrix} y_{1,1} & \cdots & y_{i,j} & \cdots & y_{n_p, p^2} \end{bmatrix}^\top$$
$$b_s = \begin{bmatrix} D_{0,1}(\beta_1) & \cdots & D_{0,j}(\beta_i) & \cdots & D_{0,p^2}(\beta_{n_p}) \end{bmatrix}^\top$$
$$A_s = \begin{bmatrix} D_{1,1}(\beta_1) & \cdots & D_{1,j}(\beta_i) & \cdots & D_{1,p^2}(\beta_{n_p}) \end{bmatrix}^\top.$$

The estimate of α is obtained using the least-squares method as follows:

$$\hat{\alpha} := A_s^\dagger (y - b_s).$$

In general, the number of pixels p^2 is greater than the number of Zernike modes n. Therefore, $\hat{\alpha}$ always exists under the assumption that $A_s \in \mathbb{R}^{(p^2 n_p) \times n}$ has full column rank (i.e., $\mathrm{rank}(A_s) = n$).

B. QP Based on the Second-Order Approximate Model

The second-order Taylor series approximation of the PSF has less model error against the actual PSF (1) in specific pixels compared with the linear approximation. Using the lifting technique in [41], (2) can be reformulated as

$$y_{i,j} = \begin{bmatrix} 1 & \alpha^\top \end{bmatrix} \begin{bmatrix} D_{0,j}(\beta_i) & \frac{1}{2} D_{1,j}(\beta_i) \\ \frac{1}{2} D_{1,j}(\beta_i)^\top & \frac{1}{2} D_{2,j}(\beta_i) \end{bmatrix} \begin{bmatrix} 1 \\ \alpha \end{bmatrix}$$

$$= \mathrm{Tr}\left(\underbrace{\begin{bmatrix} D_{0,j}(\beta_i) & \frac{1}{2} D_{1,j}(\beta_i) \\ \frac{1}{2} D_{1,j}(\beta_i)^\top & \frac{1}{2} D_{2,j}(\beta_i) \end{bmatrix}}_{\Phi_j(\beta_i)} \underbrace{\begin{bmatrix} 1 \\ \alpha \end{bmatrix} \begin{bmatrix} 1 & \alpha^\top \end{bmatrix}}_{X} \right).$$

The problem of estimating α based on the second-order Taylor series approximation can be solved using QP. The corresponding problem is formulated as follows:

$$\min_X \| y_{i,j} - \mathrm{Tr}(\Phi_j(\beta_i) X) \|^2$$
$$\text{s.t. } X_{1,1} = 1, \quad \mathrm{rank}(X) = 1, X \succeq 0$$

for all $i = 1, \ldots, n_p$ and $j = 1, \ldots, p^2$. This problem is known to be nonconvex and nondeterministic polynomial time-hard because of the rank constraint, and various approaches have been proposed to approximate the corresponding solution [42]. In this study, we reformulate the rank-constrained optimization problem into convex semidefinite programming (SDP) by replacing the rank constraint

with the ℓ_1-norm. The corresponding problem is formulated as follows:

$$\min_X \| y_{i,j} - \mathrm{Tr}(\Phi_j(\beta_i) X) \|^2 + \lambda \| X \|_1$$
$$\text{s.t. } X_{1,1} = 1, \quad X \succeq 0$$

where λ denotes a trade-off parameter between the cost function and the rank constraint. If the optimal solution X^* is determined, $\hat{\alpha}$ is obtained by rank-1 decomposition via *singular value decomposition* [43].

IV. ABERRATION CORRECTION

In this section, we propose a model predictive controller for correcting the time-varying aberrations. When the current time is k and the prediction horizon used in predictive control is N, we present $x[i|k] := x((k+i)t_s)$, $k \in \mathbb{Z}_+$, and $i = 0, 1, \ldots, N - 1$ for a signal $x(t)$ with $t \geq 0$, where t_s is the sampling interval. At each time step k, the controller computes the optimal applied voltage $\mathbf{u}^*[k] := (u^*[0|k], \ldots, u^*[N-1|k]) \in \mathbb{R}^{Nm}$ over the prediction horizon. Then, the DM is required to generate the conjugate wavefront $\phi_{\mathrm{cor}}[k] = Bu[k]$, where $u[k] = u^*[0|k]$, which corrects the input phase aberration $\phi_{\mathrm{distort}}[k+1]$ at time step $k+1$. This feedback control scheme is known as the RHC. The proposed MPC algorithm is further investigated in Section IV-B.

A. Model Identification

To determine the VAR model (3), any system identification method, such as time-series, machine learning, and extrapolation method, can be used, in principle [44], [45]. Doelman *et al.* proposed an iterative approach based on a convex heuristic to identify blind systems. To reduce the computational burden for large-scale systems, the coefficient matrix of the VAR model parametrized as the sum of the Kronecker product is estimated using an alternating least-squares method [46], [47]. In this study, we designed an AR model based on a time-series method. An open-loop wavefront dataset $\{x_t[k]|k = 1, \ldots, t_{\mathrm{train}}\}$ was used to identify the model parameters A_i as follows:

$$\underbrace{\begin{bmatrix} x_t[N_v + 1] \\ x_t[N_v + 2] \\ \vdots \\ x_t[t_{\mathrm{train}}] \end{bmatrix}^\top}_{\mathbf{x}_{\mathrm{pred}}^\top \in \mathbb{R}^{n(t_{\mathrm{train}} - N_v) \times 1}} = \underbrace{\begin{bmatrix} A_1 \\ A_2 \\ \vdots \\ A_{N_v} \end{bmatrix}^\top \begin{bmatrix} x_t[N_v] & \cdots & x_t[t_{\mathrm{train}} - 1] \\ x_t[N_v - 1] & \cdots & x_t[t_{\mathrm{train}} - 2] \\ \vdots & \ddots & \vdots \\ x_t[1] & \cdots & x_t[t_{\mathrm{train}} - N_v] \end{bmatrix}}_{\mathbf{x}_{\mathrm{past}}^\top \in \mathbb{R}^{(nN_v) \times (t_{\mathrm{train}} - N_v)}}$$

$$\therefore \mathbf{A}^\top = \begin{bmatrix} A_1 & A_2 & \cdots & A_{N_v} \end{bmatrix}^\top$$
$$= \left(\mathbf{x}_{\mathrm{past}}^\top \mathbf{x}_{\mathrm{past}} \right)^{-1} \mathbf{x}_{\mathrm{past}}^\top \mathbf{x}_{\mathrm{pred}}. \tag{7}$$

To verify the existence of (7), we assume that the number of columns of $\mathbf{x}_{\mathrm{past}}^\top$ is greater than the number of its rows, and it has full row rank (i.e., $\mathrm{rank}(\mathbf{x}_{\mathrm{past}}^\top) = nN_v$). As the order of the VAR model increases, there is a trade-off relationship between the model accuracy and simplicity, where the model
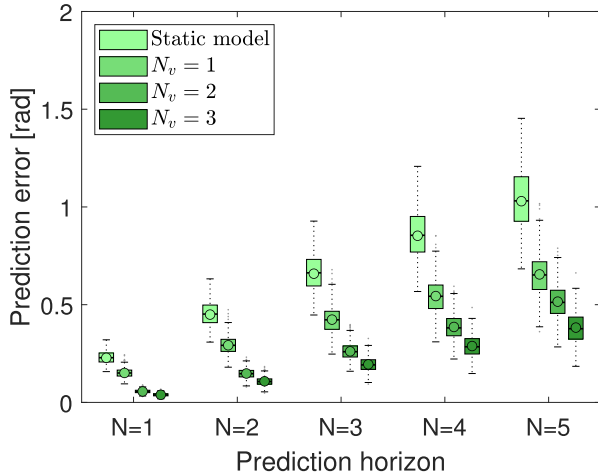
Fig. 5. Comparison of prediction error for different VAR model orders according to the prediction horizon.

TABLE I

COMPARISON OF PERFORMANCE FOR
DIFFERENT VAR MODEL ORDERS

Prediction horizon	$N = 1$	$N = 2$	$N = 3$	$N = 4$	$N = 5$
Static model [rad]	0.228	0.449	0.659	1.853	1.030
$N_v = 1$ [rad]	0.151	0.292	0.424	0.544	0.655
$N_v = 2$ [rad]	0.056	0.148	0.261	0.386	0.516
$N_v = 3$ [rad]	0.039	0.108	0.195	0.288	0.383

accuracy increases and the simplicity decreases. Fig. 5 shows the prediction error for the order of each VAR model according to the prediction horizon when the validation data for time-varying aberrations generated in Section V-A are used. The average values of the prediction error in Fig. 5 are listed in Table I. While the accuracy of the prediction model decreases as the prediction horizon increases, the prediction error reduces significantly as the order of the VAR model increases. When N_v increases from 1 to 2, the enhancements in VAR model errors according to the prediction horizon are 62.8%, 49.4%, 38.3%, 29.1%, and 21.3%, respectively. However, when N_v increases from 2 to 3, the improvements are 30.5%, 26.9%, 25.5%, 25.3%, and 25.7%, respectively, which is insignificant compared with the disadvantages caused by the increase in model complexity. Therefore, N_v was set to 2, considering the trade-off relationship between the model simplicity and accuracy.

B. Model Predictive Control

When the order of the VAR model is 2, the Zernike coefficient for the residual wavefront (5) is expressed as

$$
\begin{aligned}
x_{\text{res}}[k+1] &= x_t[k+1] + x_{\text{cor}}[k] \\
&= A_1 x_t[k] + A_2 x_t[k-1] + Bu[k] \\
&= A_1 x_{\text{res}}[k] + A_2 x_{\text{res}}[k-1] + Bu[k] \\
&\quad - A_1 Bu[k-1] - A_2 Bu[k-2].
\end{aligned} \tag{8}
$$

The constrained OCP (6) is reformulated as the MPC problem as follows:

$$
\begin{aligned}
\min_{\{\mathbf{u}[k]\}} J_k = &\sum_{i=1}^{N-1} \|x_{\text{res}}[i|k]\|_Q^2 + \|x_{\text{res}}[N|k]\|_P^2 + \sum_{i=0}^{N-1} \|u[i|k]\|_R^2 \\
\text{s.t. } &x_{\text{res}}[i+1|k] = A_1 x_{\text{res}}[i|k] + A_2 x_{\text{res}}[i-1|k] + Bu[i|k] \\
&\qquad\qquad - A_1 Bu[i-1|k] - A_2 Bu[i-2|k] \\
&u_{\min} \le u[i|k] \le u_{\max} \\
&\Delta u_{\min} \le u[i|k] - u[i-1|k] \le \Delta u_{\max} \\
&x_{\text{res}}[0|k] = \hat{x}_{\text{res}}[k], \quad x_{\text{res}}[-1|k] = \hat{x}_{\text{res}}[k-1] \\
&u[-1|k] = u[0|k-1], \quad u[-2|k] = u[0|k-2]
\end{aligned} \tag{9}
$$

where all the constraints must be satisfied for all the time indices $i = 0, 1, \ldots, N-1$. The weighting matrices for the state and input, Q and R, are listed in Table III. The weighting matrix for the terminal state P is designed as a solution to the discrete-time algebraic Riccati equation of the LQR [48]. The initial values of the state variables are estimated based on the approximate model described in Section III. The last two equality constraints imply that the previous values $u[-1|k]$ and $u[-2|k]$ for the control input at time k use the predetermined optimal control input at times $k-1$ and $k-2$, respectively.

V. NUMERICAL EXPERIMENTS

A. Simulation Setup

This section describes a case study with the time-varying phase aberrations due to atmospheric turbulence, which was generated using Object-Oriented MATLAB & Adaptive Optics (OOMAO) Toolbox [49], to validate the performance of our proposed method. To illustrate a complex environment such as the real-world atmosphere, we designed a *mainly frozen-flow* model with three layers at different heights, wind speeds, and directions [50]. This implies that the time-varying phase aberrations used in the simulation make the environment more realistic than the single-period signal used in [25]. The specific parameter values are listed in Table II. In addition, the time-varying aberrations were split into three parts, as shown in Fig. 6: 50% as the training data, 25% as the validation data, and 25% as the test data. The training data were used as an open-loop wavefront dataset to identify the VAR model described in Section IV-A. The accuracy of the identified model was evaluated using the validation data, and the test data were used in the simulations to demonstrate the effectiveness of the aberration correction of the proposed method.

To solve the MPC problem, we used the generic optimization solver SDPT3 [51] by importing it from CVX, a MATLAB package for convex optimization [52]. The specifications of the computer for the simulation are as follows: Intel Core (TM) i7-10700 CPU Hexa Core 2.90 GHz and RAM 64.00 GB. The numerical values of the control parameters are listed in Table III. These values must be carefully chosen based on the numerical experiments so that the proposed MPC method compensates for the aberrations regardless of their shape.
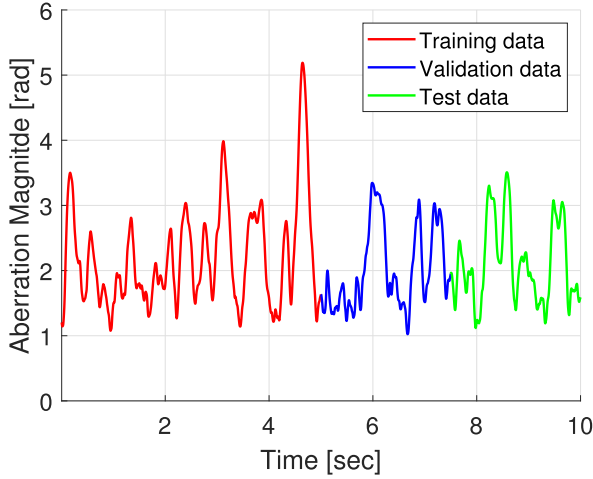
Fig. 6. Time-varying phase aberration used in the numerical experiments.

Fig. 7. Comparison of estimation error according to the aberration magnitude.

TABLE II

SIMULATION PARAMETER VALUES FOR
TIME-VARYING ABERRATION

Parameter	Meaning	Value	Unit
nRes	Resolution of camera	512	-
D	Telescope diameter	1	m
L_0	Outer scale	42	m
r_0	Fried parameter	0.1	m
h	Height	(1, 5, 12)	km
v_0	Wind speed	(5, 7.5, 10)	m/s
v_D	Wind direction	$(0, \pi/3, 5\pi/3)$	rad
f_s	Sampling frequency	200	Hz
λ	Wavelength	532	nm

TABLE III

CONTROL PARAMETER VALUES
USED IN MPC SIMULATION

Parameter	Value	Unit
p	512	-
n	28	-
m	88	-
n_p	3	-
β_i	$\pm 3, 0$	rad
N	2	-
Q	$1.5 \times 10^4 \mathbf{I}_n$	-
R	$\mathbf{I}_m$	-
SNR	10	dB
T_s	5	ms
$u_{\min}, u_{\max}$	± 200	V
$\Delta u_{\min}, \Delta u_{\max}$	± 5	V
κ	10^{-2}	-
$K^{\max}$	1	-

B. Estimation Based on Approximate PSF Model

This section describes the estimation results of the numerical simulation based on PSF approximation. The estimation error according to the aberration magnitude is shown in Fig. 7 to compare the estimation accuracy for the order of the PSF approximation model described in Section III. All 100 samples, normalized to 0.5, 1.0, and 1.5 rad rms for aberration magnitudes, were tested in a Monte Carlo simulation. The measurement noise n_i was set at a signal-to-noise ratio (SNR)
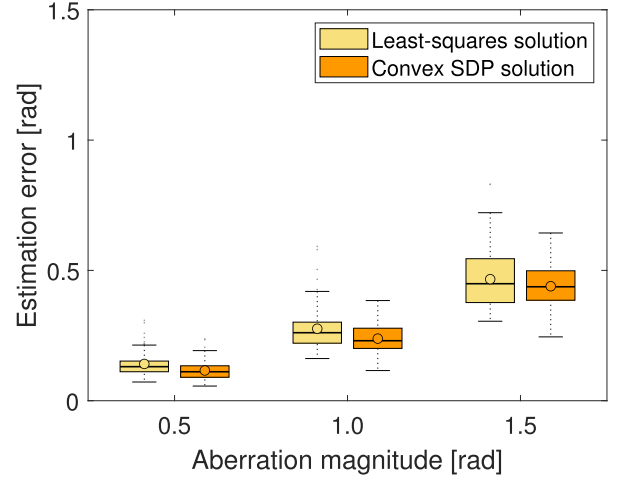

Algorithm 1 Closed-Loop Correction Process

> **for** $k = 1, ..., t_f$ **do**
>   **if** $k = 1$ **then**
> $\phi_{\mathrm{res}} \leftarrow \phi_{\mathrm{distort}}$
>   **else**
> $\phi_{\mathrm{res}} \leftarrow \phi_{\mathrm{distort}} + \phi_{\mathrm{cor}}$
>   **end if**
> $y \leftarrow |\mathcal{F}\left(\mathcal{A}(\chi) \cdot \exp\left(i\phi_{\mathrm{res}}\right)\right)|^2$
> $\hat{x}_{\mathrm{res}} \leftarrow A_s^{\dagger}(y - b_s)$ ▷ Estimator
> $x_{\mathrm{res}}[0|k] \leftarrow \hat{x}_{\mathrm{res}}$
> $\mathbf{u}^* \leftarrow \arg\min J(x_{\mathrm{res}}[0|k], \mathbf{u}[k])$ ▷ MPC
> $x_{\mathrm{cor}} \leftarrow B u^*[0|k]$
> $\phi_{\mathrm{cor}} = \mathcal{Z} \cdot x_{\mathrm{cor}}$
> **end for**

---

of 10 dB over the pupil. The estimation error and variance of the convex SDP are slightly better than those of the least-squares method. However, a least-squares solution based on a first-order approximation model was used as an estimate because the convex SDP is computationally intensive. The overall simulation procedure is outlined in Algorithm 1.

C. Comparison by VAR Model Order

In this section, we demonstrate the correction performance of the time-varying phase aberration for the proposed MPC method according to the order of the VAR model. In addition, to compare the identified model that affects the accuracy, the results obtained using a static model $A_1 = \mathbf{I}_n, A_2 = \mathbf{0}_n$ are shown in Fig. 8. When using a static model, the average value of the residual error after compensation is 0.321 rad, which means that the proposed method can provide a certain level of correction performance even if the model is inaccurate. When the first- and second-order VAR models are used, the residual error after five correction steps is reduced to 0.275 and 0.169 rad, respectively. As shown in Fig. 5, this is because the accuracy of the identified model improved as the order of the VAR model increased.
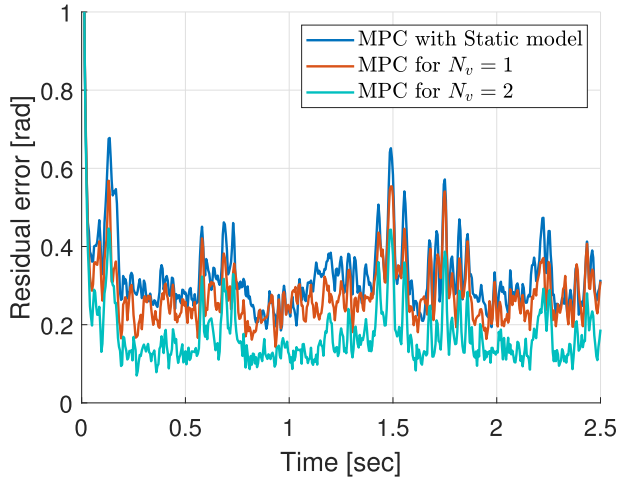
Fig. 8. Residual error in closed loop obtained by control strategies based on the time-varying phase aberration.

Fig. 9. Comparison of the residual error determined using saturation LQR and MPC.

TABLE IV

COMPARISON OF PERFORMANCE FOR DIFFERENT RAMP RATE CONSTRAINTS

Ramp constraint [V]	$\Delta u = \pm 7$	$\Delta u = \pm 6$	$\Delta u = \pm 5$
Saturation LQR [rad]	0.146	0.182	0.253
MPC [rad]	0.133	0.139	0.169
Improvement [%]	10	30.7	50

D. Saturation LQR Solution

To verify the optimality performance, we compared the solution of the proposed method with the saturation LQR solution. When there are no constraints on the control input, the optimal solution of the MPC problem (9) can be derived by considering the derivative of J_k with respect to $\mathbf{u}[k]$. Subsequently, the stroke limitation and ramp rate constraint of each actuator can be considered by simply saturating the unconstrained control input

$$\begin{cases} \max\{u_{\min}, u^*[i-1|k] + \Delta u_{\min}\} \leq u^*[i|k] \\ u^*[i|k] \leq \min\{u_{\max}, u^*[i-1|k] + \Delta u_{\max}\} \end{cases}$$

for $i = 0, 1, \ldots, N-1$. Table IV presents the average values of residual error for different ramp rate constraints obtained using the saturation LQR and our proposed method. In the extreme condition wherein the ramp rate constraint is set to a tight bound, the residual error of saturation LQR compared with MPC is increased. Fig. 9 shows the results of correction performance determined using saturation LQR and MPC for the test data shown in Fig. 6 for $\Delta u = \pm 5$ [V]. The average values of the residual error after five correction steps when using the saturation LQR and MPC are 0.253 and 0.169 rad, respectively. The saturation LQR considers the constraint sub-optimal, whereas the MPC can handle it optimally, resulting in an average 50% higher correction performance in the operation time interval.
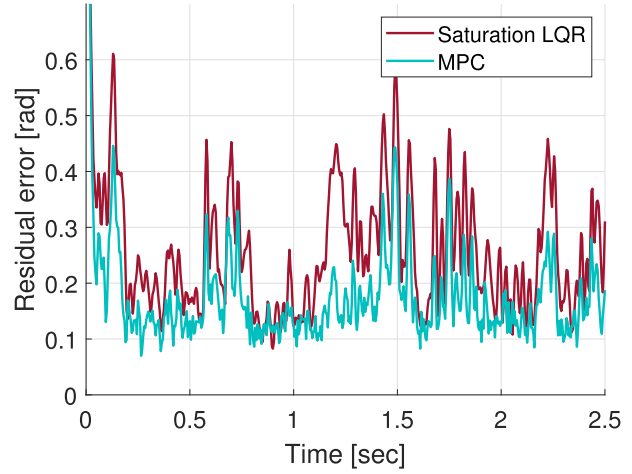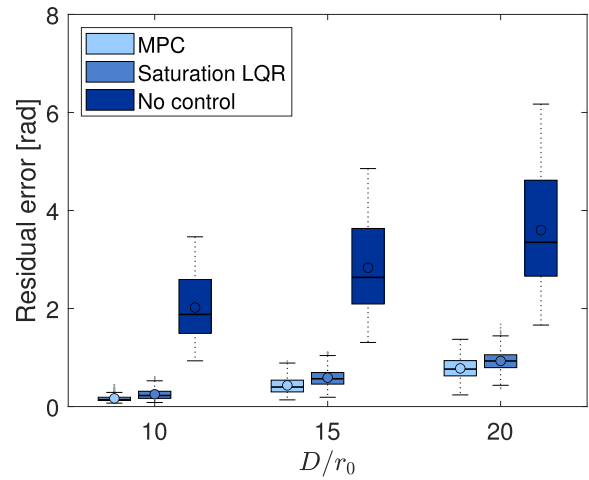

Fig. 10. Comparison of residual error in closed loop obtained using saturation LQR and MPC according to the intensity of the atmospheric turbulence.

E. Discussion With Case Studies

The results of numerical simulations will be discussed in this section. First, we verified the correction performance of the proposed method and saturation LQR for large aberrations by varying D/r_0, which represents the intensity of the atmospheric turbulence. As the value of D/r_0 increases, the strength of atmospheric turbulence intensifies as atmospheric conditions deteriorate [17]. The time-varying aberrations with $D/r_0 = 10, 15, 20$ were generated in this study by fixing the telescope diameter D and changing the Fried parameter r_0 to $0.1, 0.067, 0.05$ m. The magnitude of aberrations with different D/r_0 and the residual error compensated by the predictive control algorithm are shown in Fig. 10, and the corresponding average values are listed in Table V. The average value of the residual error after five correction steps is 0.781 rad for an aberration with a maximum magnitude of 8 rad generated when D/r_0 is increased to 20, proving that the correction performance of our proposed method is effective even for large aberrations.

TABLE V

AVERAGE VALUE OF RESIDUAL ERROR ACCORDING TO THE
INTENSITY OF THE ATMOSPHERIC TURBULENCE

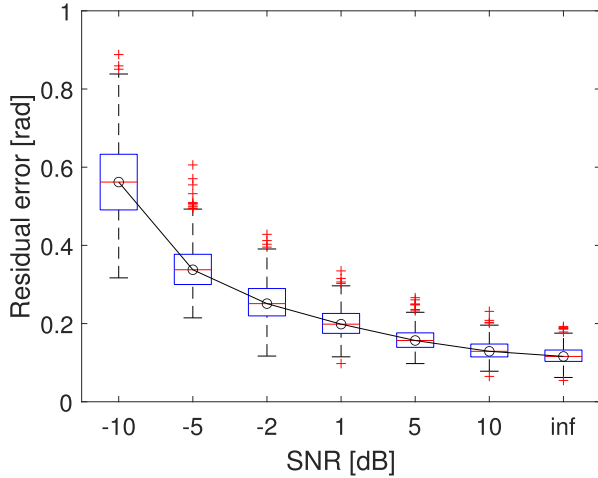| D/r_0	10	15	20
Saturation LQR [rad]	0.253	0.593	0.933
MPC [rad]	0.169	0.437	0.781

Fig. 11.   Comparison of residual error for different measurement noise levels.

TABLE VI

MEDIAN VALUE OF RESIDUAL ERROR ACCORDING TO
DIFFERENT MEASUREMENT NOISE LEVELS

SNR [dB]	-10	-5	-2	1	5	10	∞
$\|\alpha\|$ [rad]	0.569	0.344	0.256	0.202	0.160	0.132	0.119

Second, we illustrated a Monte Carlo simulation decreasing the SNR to validate the robustness to measurement noise. The effect of the camera measurement noise reduces the PSF intensity and brightness of the photon flux. Fig. 11 and Table VI show a comparison of residual error according to different measurement noise levels. When SNR = 10 dB, the residual error after five correction steps is 0.132 rad, which is similar to that in the case without measurement noise. Even if the noise level increases to SNR = 1, −2 dB, the residual errors are 0.202, 0.256 rad. Because the proposed method is insensitive to noise, it is possible to estimate the aberration of the residual wavefront from the PSF containing slight measurement noise without significant degradation of the correction performance. When the SNR is −10 dB, the residual error of the proposed method increases to 0.569 rad. In the case of measurement noise with an SNR smaller than −10 dB, the correction performance significantly deteriorates because the PSF images for estimating the Zernike coefficient are severely distorted.

F. Validation of Computational Feasibility

In this section, we verify the computational feasibility of the proposed method using fast MPC, which approximates the infeasible start primal barrier method [27]. The general

TABLE VII

COMPARISON OF PERFORMANCE
FOR DIFFERENT QP SOLVERS

	fastMPC	CVX (SDPT3)	fmincon
Residual error [rad]	0.133	0.132	0.132
Computation time [sec]	0.003	0.215	0.152

primal barrier method replaces the inequality constraints with a barrier function in the objective function and finds a solution while reducing the barrier parameter κ. When the barrier parameter has a certain value, the solution to the convex optimization problem with linear equality constraints can be obtained using Newton's method. To reduce the computational burden of the barrier method, the authors of [27] presented simple variations that fix κ and the Newton iteration step K^{max}. Table III lists the numerical values of the barrier parameter and iteration limit based on numerous numerical simulations. The results of using fast MPC to correct the time-varying aberrations are compared with those of a generic optimization solver such as SDPT3 called by CVX and built-in function `fmincon` in MATLAB. The stroke limitation of the DM was considered for the constraints on the applied voltage of each actuator. Table VII presents the residual error and computation time determined using different QP solvers for the time-varying aberrations shown in Fig. 6. For each solver, no significant difference was observed in the average values of residual errors after five correction steps; however, in terms of computation time, fast MPC was 80 and 60 times faster than CVX and `fmincon`, respectively. This implies that the proposed method can be implemented in real-time for an AO system. The MATLAB code for our simulation is available online [53].

VI. Conclusion and Future Work

This study presented an MPC method to compensate for the time-varying aberrations in sensorless AO. To estimate aberrations without using a wavefront sensor, we mathematically derived a PSF approximation model based on the Taylor series expansion around zero aberration. The proposed controller explicitly considers the operating limits of actuators for the stable and reliable operation of a DM. We designed an AR model based on a time-series method to identify the VAR model of the time-varying aberrations. Numerical case studies were presented to verify the correction performance of the AR model according to the VAR order and to demonstrate the computational efficiency and optimality performance of our MPC according to the magnitude of aberration and measurement noise level. In addition, we used fast MPC, an algorithm that fixes the barrier parameters and the Newton steps of the interior-point method, to solve the resultant constrained OCP to be feasible in real-time. In future work, we will consider the improvement of estimation accuracy of the phase diversity method for large-phase aberrations, which assumes small-phase aberrations. Moreover, uncertainties in the AO system and dynamic models need to be carefully investigated. In addition, a robust MPC that satisfies the stability and

performance criteria for model uncertainties in the form of bounded input disturbances needs to be investigated.

APPENDIX

A. Derivative of PSF Approximate Model

In this section, the first and second derivatives of the approximate model are derived. The uth element of $D_{1,j}(\beta_i)$ is

$$D_{1,j}(\beta_i)_u = \left.\frac{\partial y_j(\zeta; \alpha, \beta_i)}{\partial \alpha_u}\right|_{\alpha=0} \quad \forall u = 1, \ldots, n.$$

Applying the product rule to (1)

$$\frac{\partial y_j(\zeta; \alpha, \beta_i)}{\partial \alpha_u} = \frac{\partial \mathcal{F}(g(\chi; \alpha, \beta_i))}{\partial \alpha_u}\mathcal{F}(g(\chi; \alpha, \beta_i))^*$$
$$+ \mathcal{F}(g(\chi; \alpha, \beta_i))\frac{\partial \mathcal{F}(g(\chi; \alpha, \beta_i))^*}{\partial \alpha_u}$$
$$= 2\Re\left[\frac{\partial \mathcal{F}(g(\chi; \alpha, \beta_i))}{\partial \alpha_u}\mathcal{F}(g(\chi; \alpha, \beta_i))^*\right]. \quad (10)$$

The $\Re(\cdot)$ and $\Im(\cdot)$ operators denote the real and imaginary parts of a complex number, respectively. The first derivative of the Fourier transform of the GPF is

$$\frac{\partial \mathcal{F}(g(\chi; \alpha, \beta_i))}{\partial \alpha_u} = \frac{\partial}{\partial \alpha_u}\left[\mathcal{F}(\mathcal{A}(\chi) \cdot \exp(i\phi_i(\chi)))\right]$$
$$= i\mathcal{F}(g(\chi; \alpha, \beta_i)Z_u(\chi)). \quad (11)$$

By combining (10) and (11), the derivative of α_u with respect to the PSF corresponding to the jth pixel is given by

$$\frac{\partial y_j(\zeta; \alpha, \beta_i)}{\partial \alpha_u} = 2\Re\left[i\mathcal{F}(g(\chi; \alpha, \beta_i)Z_u(\chi))\mathcal{F}(g(\chi; \alpha, \beta_i))^*\right]$$
$$= -2\Im\left[\mathcal{F}(g(\chi; \alpha, \beta_i)Z_u(\chi))\mathcal{F}(g(\chi; \alpha, \beta_i))^*\right].$$

Based on the first derivative described above, the second derivative can be derived as follows: The element at the uth row and vth column of $D_{2,j}(\beta_i)$ is

$$D_{2,j}(\beta_i)_{u,v} = \left.\frac{\partial^2 y_j(\zeta; \alpha, \beta_i)}{\partial \alpha_u \partial \alpha_v^\top}\right|_{\alpha=0} \quad \forall u, v = 1, \ldots, n.$$

The derivative of α_u and α_v with respect to the PSF corresponding to the jth pixel is expressed as

$$\frac{\partial^2 y_j(\zeta; \alpha, \beta_i)}{\partial \alpha_u \partial \alpha_v^\top} = 2\Re\left[\frac{\partial^2 \mathcal{F}(g(\chi; \alpha, \beta_i))}{\partial \alpha_u \partial \alpha_v^\top} \cdot \mathcal{F}(g(\chi; \alpha, \beta_i))^*\right.$$
$$\left. + \frac{\partial \mathcal{F}(g(\chi; \alpha, \beta_i))}{\partial \alpha_u}\frac{\partial \mathcal{F}(g(\chi; \alpha, \beta_i))^*}{\partial \alpha_v^\top}\right]. \quad (12)$$

The second derivative of the Fourier transform of the GPF is

$$\frac{\partial^2 \mathcal{F}(g(\chi; \alpha, \beta_i))}{\partial \alpha_u \partial \alpha_v^\top} = -\mathcal{F}(g(\chi; \alpha, \beta_i)Z_u(\chi)Z_v(\chi)).$$

Therefore, (12) can be rewritten as

$$\frac{\partial^2 y_j(\zeta; \alpha, \beta_i)}{\partial \alpha_u \partial \alpha_v^\top}$$
$$= 2\Re\left[\mathcal{F}(g(\chi; \alpha, \beta_i)Z_u(\chi))\mathcal{F}(g(\chi; \alpha, \beta_i)Z_v(\chi))^*\right.$$
$$\left. - \mathcal{F}(g(\chi; \alpha, \beta_i)Z_u(\chi)Z_v(\chi))\mathcal{F}(g(\chi; \alpha, \beta_i))^*\right].$$

REFERENCES

[1] M. J. Booth, "Adaptive optical microscopy: The ongoing quest for a perfect image," *Light, Sci. Appl.*, vol. 3, no. 4, p. e165, 2014.

[2] M. J. Booth, "Adaptive optics in microscopy," *Phil. Trans. Roy. Soc. A, Math., Phys. Eng. Sci.*, vol. 365, no. 1861, pp. 2829–2843, 2007.

[3] P. Zhou, Y. Ma, X. Wang, H. Ma, X. Xu, and Z. Liu, "Coherent beam combination of three two-tone fiber amplifiers using stochastic parallel gradient descent algorithm," *Opt. Lett.*, vol. 34, pp. 2939–2941, Oct. 2009.

[4] H. Ma, Z. Liu, X. Xu, and J. Chen, "Simultaneous adaptive control of dual deformable mirrors for full-field beam shaping with the improved stochastic parallel gradient descent algorithm," *Opt. Lett.*, vol. 38, no. 3, pp. 326–328, 2013.

[5] P. Yang, M. Ao, Y. Liu, B. Xu, and W. Jiang, "Intracavity transverse modes controlled by a genetic algorithm based on Zernike mode coefficients," *Opt. Exp.*, vol. 15, pp. 17051–17062, Dec. 2007.

[6] Y. Liu, J. Ma, B. Li, and J. Chu, "Hill-climbing algorithm based on Zernike modes for wavefront sensorless adaptive optics," *Opt. Eng.*, vol. 52, no. 1, 2013, Art. no. 016601.

[7] Y. Liu, J. Ma, J. Chen, B. Li, and J. Chu, "Robustness properties of hill-climbing algorithm based on Zernike modes for laser beam correction," *Appl. Opt.*, vol. 53, pp. B140–B146, Apr. 2014.

[8] W. Lianghua *et al.*, "Synchronous model-based approach for wavefront sensorless adaptive optics system," *Opt. Exp.*, vol. 25, pp. 20584–20597, Aug. 2017.

[9] M. J. Booth, "Wave front sensor-less adaptive optics: A model-based approach using sphere packings," *Opt. Exp.*, vol. 14, no. 4, pp. 1339–1352, 2006.

[10] H. Linhai and C. Rao, "Wavefront sensorless adaptive optics: A general model-based approach," *Opt. Exp.*, vol. 19, pp. 371–379, Jan. 2011.

[11] R. A. Gonsalves, "Phase retrieval and diversity in adaptive optics," *Opt. Eng.*, vol. 21, no. 5, pp. 829–832, Oct. 1982.

[12] R. G. Paxman, T. J. Schulz, and J. R. Fienup, "Joint estimation of object and aberrations by using phase diversity," *J. Opt. Soc. Amer. A, Opt. Image Sci.*, vol. 9, no. 7, pp. 1072–1085, Jul. 1992.

[13] A. P. Krishnan, C. Belthangady, C. Nyby, M. Lange, B. Yang, and L. A. Royer, "Optical aberration correction via phase diversity and deep learning," *BioRxiv*, Apr. 2020, doi: 10.1101/2020.04.05.026567.

[14] C. S. Smith *et al.*, "Iterative linear focal-plane wavefront correction," *J. Opt. Soc. Amer. A, Opt. Image Sci.*, vol. 30, pp. 2002–2011, Oct. 2013.

[15] W. J. Wild, "Linear phase retrieval for wave-front sensing," *Opt. Lett.*, vol. 23, pp. 573–575, Apr. 1998.

[16] C. Smith, R. Marinica, and M. Verhaegen, "Real-time wavefront reconstruction from intensity measurements," in *Proc. 3rd AO4ELT Conf.*, S. Esposito and L. Fini, Eds. Dec. 2013, p. 30.

[17] D. Yue, H. Nie, Y. Li, and C. Ying, "Fast correction approach for wavefront sensorless adaptive optics based on a linear phase diversity technique," *Appl. Opt.*, vol. 57, pp. 1650–1656, Mar. 2018.

[18] D. Yue and H. Nie, "Wavefront sensorless adaptive optics system for extended objects based on linear phase diversity technique," *Opt. Commun.*, vol. 475, Nov. 2020, Art. no. 126209.

[19] R. Doelman, M. Klingspor, A. Hansson, J. Löfberg, and M. Verhaegen, "Identification of the dynamics of time-varying phase aberrations from time histories of the point-spread function," *J. Opt. Soc. Amer. A, Opt. Image Sci.*, vol. 36, pp. 809–817, May 2019.

[20] R. Marinica, C. S. Smith, and M. Verhaegen, "State feedback control with quadratic output for wavefront correction in adaptive optics," in *Proc. 52nd IEEE Conf. Decis. Control*, 2013, pp. 3475–3480.

[21] K. Hinnen, M. Verhaegen, and N. Doelman, "A data-driven H_2-optimal control approach for adaptive optics," *IEEE Trans. Control Syst. Technol.*, vol. 16, no. 3, pp. 381–395, May 2008.

[22] J. M. Maciejowski, *Predictive Control: With Constraints*. London, U.K.: Pearson, 2002.

[23] P. O. M. Scokaert and J. B. Rawlings, "Constrained linear quadratic regulation," *IEEE Trans. Autom. Control*, vol. 43, no. 8, pp. 1163–1169, Aug. 1998.

[24] D. Q. Mayne, J. B. Rawlings, C. V. Rao, and P. O. M. Scokaert, "Constrained model predictive control: Stability and optimality," *Automatica*, vol. 36, no. 6, pp. 789–814, 2000.

[25] M. Glück, J.-U. Pott, and O. Sawodny, "Model predictive control of multi-mirror adaptive optics systems," in *Proc. IEEE Conf. Control Technol. Appl. (CCTA)*, Aug. 2018, pp. 909–914.

[26] M. V. Konnik and J. De Doná, "Feasibility of constrained receding horizon control implementation in adaptive optics," *IEEE Trans. Control Syst. Technol.*, vol. 23, no. 1, pp. 274–289, Jan. 2015.

[27] Y. Wang and S. Boyd, "Fast model predictive control using online optimization," *IEEE Trans. Control Syst. Technol.*, vol. 18, no. 2, pp. 267–278, Mar. 2010.

[28] P. Riaud, D. Mawet, and A. Magette, "Nijboer-Zernike phase retrieval for high contrast imaging-principle, on-sky demonstration with NACO, and perspectives in vector vortex coronagraphy," *Astron. Astrophys.*, vol. 545, p. A150, Sep. 2012.

[29] P. Zhang, C. Yang, Z. Xu, Z. Cao, Q. Mu, and L. Xuan, "High-accuracy wavefront sensing by phase diversity technique with bisymmetric defocuses diversity phase," *Sci. Rep.*, vol. 7, no. 1, pp. 1–10, 2017.

[30] L. N. Thibos, R. A. Applegate, J. T. Schwiegerling, and R. Webb, "Standards for reporting the optical aberrations of eyes," *Vis. Sci. Appl.*, vol. 35, pp. 232–244, Feb. 2000.

[31] B. H. Dean and C. W. Bowers, "Diversity selection for phase-diverse phase retrieval," *J. Opt. Soc. Amer. A, Opt. Image Sci.*, vol. 20, pp. 1490–1504, Aug. 2003.

[32] R. A. Gonsalves, "Small-phase solution to the phase-retrieval problem," *Opt. Lett.*, vol. 26, pp. 684–685, May 2001.

[33] B. Zhang, J. Zerubia, and J.-C. Olivo-Marin, "Gaussian approximations of fluorescence microscope point-spread function models," *Appl. Opt.*, vol. 46, no. 10, pp. 1819–1829, 2007.

[34] J. Silva, E. Brunner, A. Polo, C. de Visser, and M. Verhaegen, "Wavefront reconstruction using intensity measurements for real-time adaptive optics," in *Proc. Eur. Control Conf. (ECC)*, 2014, pp. 2412–2417.

[35] D. J. Lee, M. C. Roggemann, and B. M. Welsh, "Cramér–Rao analysis of phase-diverse wave-front sensing," *J. Opt. Soc. Amer. A, Opt. Image Sci.*, vol. 16, pp. 1005–1015, May 1999.

[36] P. Piscaer, O. Soloviev, and M. Verhaegen, "Phase retrieval of large-scale time-varying aberrations using a non-linear Kalman filtering framework," *J. Opt. Soc. Amer. A, Opt. Image Sci.*, vol. 38, pp. 25–35, Jan. 2021.

[37] L. Huang, C. Rao, and W. Jiang, "Modified Gaussian influence function of deformable mirror actuators," *Opt. Exp.*, vol. 16, pp. 108–114, Jan. 2008.

[38] H. Gonzalez-Nunez, C. Bechet, B. Ayancan, B. Neichel, and A. Guesalaga, "Effect of the influence function of deformable mirrors on laser beam shaping," *Appl. Opt.*, vol. 56, no. 6, pp. 1637–1646, 2017.

[39] J. Alda and G. D. Boreman, "Zernike-based matrix model of deformable mirrors: Optimization of aperture size," *Appl. Opt.*, vol. 32, pp. 2431–2438, May 1993.

[40] B. P. Wallace, P. J. Hampton, C. H. Bradley, and R. Conan, "Evaluation of a MEMS deformable mirror for an adaptive optics test bench," *Opt. Exp.*, vol. 14, no. 22, pp. 10132–10138, 2006.

[41] H. Ohlsson, A. Y. Yang, R. Dong, M. Verhaegen, and S. Sastry, "Quadratic basis pursuit," 2013, *arXiv:1301.7002*.

[42] B. K. Natarajan, "Sparse approximate solutions to linear systems," *SIAM J. Comput.*, vol. 24, no. 2, pp. 227–234, Feb. 1995.

[43] R. A. Beezer, *A First Course in Linear Algebra*. Congruent Press, 2012.

[44] P. Piscaer, O. Soloviev, and M. Verhaegen, "Predictive wavefront sensorless adaptive optics for time-varying aberrations," *J. Opt. Soc. Amer. A, Opt. Image Sci.*, vol. 36, pp. 1810–1819, Nov. 2019.

[45] M. Verhaegen and V. Verdult, *Filtering and System Identification: A Least Squares Approach*. Cambridge, U.K.: Cambridge Univ. Press, 2007.

[46] G. Monchen, B. Sinquin, and M. Verhaegen, "Recursive Kronecker-based vector autoregressive identification for large-scale adaptive optics," *IEEE Trans. Control Syst. Technol.*, vol. 27, no. 4, pp. 1677–1684, Jul. 2019.

[47] B. Sinquin and M. Verhaegen, "Quarks: Identification of large-scale Kronecker vector-autoregressive models," *IEEE Trans. Autom. Control*, vol. 64, no. 2, pp. 448–463, Feb. 2019.

[48] B. Kouvaritakis and M. Cannon, *Model Predictive Control*. Cham, Switzerland: Springer, 2016, p. 38.

[49] R. Conan and C. Correia, "Object-oriented MATLAB adaptive optics toolbox," in *Proc. SPIE*, vol. 9148, E. Marchetti, L. M. Close, and J.-P. Vran, Eds. Aug. 2014, Art. no. 91486C.

[50] L. Prengère, C. Kulcsár, and H.-F. Raynaud, "Zonal-based high-performance control in adaptive optics systems with application to astronomy and satellite tracking," *J. Opt. Soc. Amer. A, Opt. Image Sci.*, vol. 37, pp. 1083–1099, Jul. 2020.

[51] K.-C. Toh, M. J. Todd, and R. H. Tütüncü, "SDPT3—A MATLAB software package for semidefinite programming, version 1.3," *Optim. Methods Softw.*, vol. 11, nos. 1–4, pp. 545–581, 1999.

[52] M. Grant and S. Boyd. (Mar. 2014). *CVX: MATLAB Software for Disciplined Convex Programming, Version 2.1*. [Online]. Available: http://cvxr.com/cvx

[53] J. Kim *et al.* (Oct. 2021). *Model Predictive Control Simulation Package for Sensorless Adaptive Optics in MATLAB*. [Online]. Available: https://github.com/jinsungkim96/MPC-SensorlessAO